Journal of Power Sources 613 (2024) 234802

Contents lists available at ScienceDirect

Journal of Power Sources

journal homepage: www.elsevier.com/locate/jpowsour

Highly active bimetallic nanocatalysts (Pd/Ag and Pd/ZnO) decorated nitrogen-doped onion-like carbon nanoparticles for enhanced methanol oxidation in alkaline media

Ludwe L. Sikeyi [a,b], Themba D. Ntuli [a], Nobanathi W. Maxakato [c], Neil J. Coville [a,d], Manoko S. Maubane-Nkadimeng [a,d,e,*]

[a] Molecular Sciences Institute, School of Chemistry, University of Witwatersrand, Braamfontein, 2050, South Africa
[b] Institute for the Catalysis and Energy Solutions (ICES), College of Engineering, Science and Technology, University of South Africa, Florida Science Campus, Roodepoort 1709, South Africa
[c] Department of Chemical Science, University of Johannesburg, Doornfontein, 2021, South Africa
[d] DSI-NRF Centre of Excellence in Strong Materials, University of Witwatersrand, Braamfontein, 2050, South Africa
[e] Microscopy and Microanalysis Unit, University of Witwatersrand, Braamfontein, 2050, South Africa

HIGHLIGHTS

- *N*-OLCNs with rich defective sites were synthesized using a flame pyrolysis method.
- Pd-based electrocatalysts were prepared by the sodium borohydride reduction method.
- Nitrogen doping facilitated the attachment of Pd, Ag, and ZnO onto the OLCNs.
- The catalysts exhibit superior catalytic activity and excellent stability in MOR.

GRAPHICAL ABSTRACT

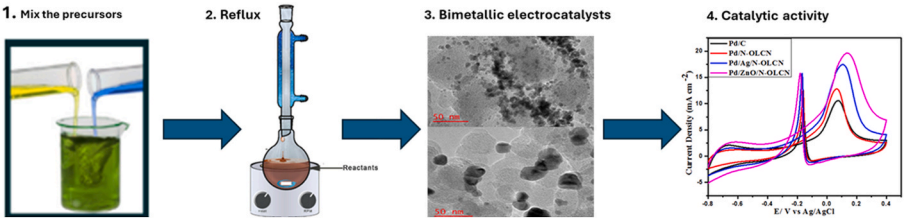

ARTICLE INFO

Keywords:
Cyclic voltammetry
Direct methanol fuel cell
Electrocatalysts
Nitrogen doping
Onion-like carbon nanoparticles

ABSTRACT

Nitrogen-doped onion-like carbons (N-OLCNs) rich with defective sites are synthesized using a flame pyrolysis method, using acetonitrile as both carbon and nitrogen sources. Bimetallic (Pd/Ag and Pd/ZnO) electrocatalysts prepared in a one-pot method using sodium borohydride as a reducing agent, are supported on the N-OLCNs. X-ray diffraction data shows the formation of Pd/Ag and Pd/ZnO supported on the N-OLCNs surface. Transmission electron microscopy analysis confirms the existence of well-dispersed, spherically shaped Pd/Ag (16.9 ± 4.8 nm) and Pd/ZnO (10.4 ± 1.0 nm) on the surface of the N-OLCNs. Pd/N-OLCN, Pd/Ag/N-OLCN, Pd/ZnO/N-OLCN, and a Pd/C electrocatalyst are studied in the methanol oxidation reaction (MOR). Incorporating Ag and ZnO improves the Pd/N-OLCN physiochemical properties and catalytic performance towards MOR in alkaline electrolyte. The Pd/Ag/N-OLCN and Pd/ZnO/N-OLCN electrocatalysts exhibit superior anti-poisoning tolerance, better electrocatalytic stability, and fast charge transfer resistance as compared to monometallic Pd/N-OLCN and Pd/C electrocatalysts in MOR. It is proposed that the electron transfer from the Ag species to the Pd modified the active sites of Pd by increasing the electron density at Pd and hence promoting the desorption of methanol. Furthermore, the improved catalytic performance could also be related to a strong metal-support interaction.

* Corresponding author.
E-mail address: manoko.maubane@wits.ac.za (M.S. Maubane-Nkadimeng).

https://doi.org/10.1016/j.jpowsour.2024.234802
Received 29 February 2024; Received in revised form 22 April 2024; Accepted 27 May 2024

1. Introduction

The issue of energy, its generation, storage, and use, has become one of the most important technological problems facing societies as reflected in one of the United Nations Sustainable Development Goals (SDG #7) [1]. In the recent past, much of society's energy has been created from fossil fuels (oil/gas/coal) but it is clear that this is unsustainable and that alternatives to energy production from renewable sources are needed [2]. There are a variety of approaches to achieve this aim, and fuel cells represent one of these avenues to provide clean energy production and sustainable power generation. Their continuous development and implementation are critical to the transition to a more sustainable future. Indeed, fuel cell technology is not new, and these devices have been used in space probes, satellites, and manned spacecraft for decades [3]. Furthermore, thousands of stationary fuel cell systems have been installed in utility power plants, hotels, and schools for both primary and backup power [4]. Numerous types of fuel cells have been developed to provide energy and one of these that has shown promise is the direct methanol fuel cell (DMFC).

The advantages of using DMFCs include that they have a high energy density, safe to operate, environmentally friendly, and the fuel is easy to transport [5]. DMFCs use methanol, an energy-dense stable low molecular weight alcohol as a fuel [6]. DMFCs are promising sources of clean energy for portable devices, however, there are two significant issues associated with DMFCs: a high methanol membrane crossover and a very large overpotential for the methanol oxidation reaction [7]. These issues have been addressed by many past and ongoing studies involving both membrane and catalyst developments. Indeed, the development of highly active and stable electrocatalysts for the electrooxidation of methanol in DMFCs has become the subject of many researchers [8–10].

The oxidation kinetics of methanol is faster in alkaline electrolytes such as potassium hydroxide or sodium hydroxide, as compared to acid electrolytes such as sulphuric acid [11]. The basic media allows for utilizing cost-effective metal-based electrocatalysts that can facilitate the development of the DMFC [12]. Thus, much recent research has been directed at reducing platinum usage in alkaline conditions. In particular, Pd-based nanostructured electrocatalysts have been shown to be excellent catalysts in methanol oxidation reactions in alkaline conditions [13]. The use of palladium in the commercialization of DMFCs is, however, limited due to its expense. Alloying Pd catalysts with cheaper metals like Zn, Fe, Ag, Co, and Ni is one approach used to form less expensive bimetallic catalysts for the methanol electro-oxidation reaction in alkaline media [14,15]. Furthermore, nanocatalysts with two metals have shown enhanced catalytic activity when compared to their monometallic counterparts [16]. It has also been observed that alloying Pd with a metal of a smaller lattice constant is expected to result in a Pd lattice contraction, which will moderate the oxygen species chemisorptive bond strength [17]. For example, Wang et al. reported on the use of bimetallic Pd–Ag/C nanocatalysts with different carbon support materials (prepared by a borohydride reduction method), for methanol oxidation reactions (MOR) in alkaline media. The Pd–Ag (1:1)/carbon nanotubes (CNTs) electrocatalyst exhibited higher catalytic activity as compared to Pd–Ag (1:1)/carbon black and the commercial Pd/C in MOR. This was suggested to be due to a higher specific surface area and larger pore volume of activated CNTs as compared to carbon black [18]. Kien et al. synthesized intermetallic (i) and substitutional solid-solution (s) PdZn alloy nanoparticle (NP)-loaded carbon black (i-PdZn/C and *s*-PdZn/C) by heat treatment in an autoclave at 220 °C for 24 h. The i-PdZn/C and *s*-PdZn/C bimetallic electrocatalysts showed better ethanol oxidation reaction (EOR) activity than Pd/C electrocatalyst, in 1 M KOH electrolyte. The enhanced EOR activity is due to the electronic effect and increased surface area of the bimetallic electrocatalysts [19]. Thus, studies have shown that combining Pd with Zn and Ag not only changes the properties of Pd, and enhances its activity and resistance, but also reduces the cost of the electrodes for the use of Pd electrocatalysts in DMFCs.

Carbon support materials play a major role in enhancing the catalytic activity of the electrocatalysts and have been used in a wide range of applications such as in supercapacitors, electrochemical catalysis, energy storage, sensors, and water treatment [20–22]. This includes their use in direct alcohol fuel cells. For these applications, the carbons are required to possess a large external surface area, nanoscopic size, high electrical conductivity, large-scale synthesis, and excellent tribological behavior [23]. A carbon nanomaterial that has been used is that with a spherical shape. The quasi-spherical nanostructure, the concentric graphene shells, and graphitic defects of carbon can enhance the chemical reactivity of spherical carbons [24]. The spherically shaped carbon family includes both carbon nano onions (CNOs) and their associated onion-like nano-carbon counterparts (OLCNs); many OLCNs are often referred to as CNOs even though they do not have a true onion-like structure. These CNOs/OLCNs have been employed as catalyst supports in fuel cells [25]. The electronic transport and structure of CNOs/OLCNs can be tailored by heteroatom doping. In particular, the existence of nitrogen heteroatoms in the spherical structure can strongly improve the electrocatalytic activity of the carbon through Faradaic redox reactions created by graphitic-N, pyrrolic N (N–H), pyridinic-N and pyridinic N^{+}–O^{-} [26] bonds. Furthermore, nitrogen doping increases the charge carrier density, specific surface area, and electron transport of carbons [27]. The nitrogen doping into the sp^2-hybridized carbon structure can modify their surface chemical activities, electronic structures and provide an alternative strategy to improve the catalytic activity of the electrocatalyst [28].

This study has focused on improving the direct methanol alkaline fuel cell (DMAFC) performance by using both N-doped OLCNs and bimetallic Pd catalysts (Pd/Ag/N-OLCN and Pd/ZnO/N-OLCN) in a basic (sodium hydroxide) electrolyte. N-OLCNs were synthesized by a flame pyrolysis method in one step using acetonitrile as a carbon source and a nitrogen precursor [24]. The bimetallic Pd–Ag, Pd–ZnO, and monometallic Pd nanoparticles, supported over the N-OLCNs, were prepared utilizing a one pot synthesis method. The ternary Pd/ZnO/N-OLCN electrocatalyst exhibited superior catalytic activity, excellent electrochemical stability, and fast electron transfer for methanol oxidation reactions in alkaline media when compared to Pd/Ag/N-OLCN, Pd/N-OLCN and commercial Pd/C electrocatalysts. A proposal to explain the observations is reported.

2. Experimental procedures

2.1. Materials and reagents

The following chemicals were all of analytical grade and were purchased from Sigma-Aldrich, South Africa: sodium borohydride (>99.5 %), Nafion solution (>5 wt%), palladium chloride (>98.0 %), silver chloride (>98.0 %), zinc chloride (>98.0 %), Pd/C commercial standard (>10 % loading), acetonitrile (>99.5 %), sodium hydroxide pellets and methanol (>99.9 %).

2.2. Synthesis of nitrogen-doped onion-like carbon nanoparticles (N-OLCNs)

N-OLCN nanoparticles were prepared using the flame pyrolysis-assisted method as previously reported [24]. In summary, a required quantity of acetonitrile was placed in a 100 mL glass beaker and ignited in the air under carefully monitored fume hood conditions to prevent the emission of any harmful gases during flaming. Acetonitrile served as a nitrogen and carbon source in this instance. This method involved in-situ heteroatom doping in a single step without the need for severe post-doping chemical treatments. The set-up was made to collect the carbon particles as they were produced. No post-processing or purification was undertaken (yield 3.5 %).

2.3. Synthesis of Ag/N-OLCN, ZnO/N-OLCN, Pd/N-OLCN, Pd/Ag/N-OLCN and Pd/ZnO/N-OLCN electrocatalysts

The palladium-based electrocatalysts were synthesized using a one-pot synthesis method [29]. The 1 M sodium borohydride ($NaBH_4$) stock solution was prepared by adding the dry granulated $NaBH_4$ to the 1.0 N sodium hydroxide (NaOH) solution under stirring conditions until a homogeneous mixture was formed. Typically, 200 mg of N-OLCNs were mixed with a 20 mL sodium borohydride solution under continuous stirring for 30 min. To this was added $AgCl_2$ (13.3 mg), (or $ZnCl_2$ (20.8 mg)) and $PdCl_2$ (16.9 mg) to give 5 % weight loaded Ag/N-OLCN, ZnO/N-OLCN, Pd/N-OLCN. The mixtures were each refluxed at 100 °C for 6 h. Bimetallic catalysts containing 6 % Pd:4 % Ag and 6 % Pd:4 % ZnO, to give a 10 % overall %weight loading, were made similarly. The reaction mixture became dark grey within several minutes under reflux. The obtained slurries were centrifuged at 6000 rpm for 25 min and rinsed with double distilled water to remove residual chloride. The obtained monometallic and bimetallic (Ag/N-OLCN, ZnO/N-OLCN, Pd/N-OLCN, Pd/Ag/N-OLCN, and Pd/ZnO/N-OLCN**)** electrocatalysts were then dried in an oven at 100 °C for 24 h.

2.4. Physicochemical characterization

Transmission electron microscopy (TEM) using a JEOL JEM-2100 F, operated at a voltage of 200 kV was used to study the microstructure, morphology and the selected area electron diffraction (SAED) of the prepared samples. Scanning electron microscopy (SEM) using ZEISS Sigma 300 V P Oxford Field Emission equipment was used to obtain surface micrographs and energy-dispersive X-ray (EDS) images. Thermogravimetric (TGA) analysis was performed on a PerkinElmer 6000 to study the thermal stability of the samples. A Micrometrics Tristar 3000 surface area and porosity analyzer were used to elucidate the surface area pore volume, and pore size of the prepared samples, using the Brunauer-Emmett-Teller (BET) method. A Bruker D2 Phaser diffractometer with a Cu Kα radiation source generated at 30 kV was used to measure the Powder X-ray diffraction (XRD) patterns of the samples. X-ray photoelectron spectroscopy (XPS), using a Thermo Scientific ESCALAB 250Xi spectrometer operating with an X-ray power of 300 W, was used to measure the elemental composition of the surface of the samples.

2.5. Electrochemical characterization

The electrochemical experiments were performed with a Dropsens potentiostat. For these experiments, a standard three-electrode cell was employed using a glassy carbon (GC) electrode (geometrical surface area of 0.196 cm^2) as support for the working electrode and a platinum wire and a saturated silver chloride electrode (Ag/AgCl), as counter and reference electrodes, respectively. The working electrode was constructed by dispersing 10 mg of each electrocatalyst powder in a solution composed of 1 mL of ethanol and 5 μL of a 5 wt% Nafion solution. This mixture was then placed in an ultrasonic bath for 15 min to produce a black electrocatalyst ink. Then 15 μL of the ink was transferred to the glassy carbon electrode support and dried at room temperature. About 0.052 mg cm^{-2} of Pd was loaded onto the nanocatalysts on the glassy carbon electrode. The electrolyte solution was purged with argon for 15 min before conducting electrochemical experiments to remove any oxygen in the solution. Cyclic voltammetry (CV), chronoamperometry (CA), and electrochemical impedance spectroscopy (EIS) measurements were carried out in argon-saturated solutions containing 1 M NaOH and 1 M CH_3OH. The electrochemical surface area (ECSA) measurements of the Pd-based nanocatalysts were normalized using the working electrode's geometric surface area. The ECSA of the palladium-based electrocatalysts was used to normalize the currents obtained in the CV, CA, and EIS tests.

3. Results and discussion

3.1. Physicochemical properties of N-OLCN and the nanocatalysts

3.1.1. Transmission electron microscopy and energy dispersive X-ray spectroscopy mapping

Fig. S1 displays the TEM micrographs of the N-OLCN (inset SAED image), Pd/N-OLCN Ag/N-OLN, and ZnO/N-OLCN. Fig. S1(a) reveals concentric turbostratic shells for the N-OLCN with an interplanar spacing of ca. 0.33 nm [30] and the SAED image confirmed that the material was amorphous. As shown in Fig. S1(b) the palladium nanoparticles were evenly distributed onto the N-OLCN surface [30]. The average Pd crystallite size of Pd/N-OLCN was determined from TEM images to be 4.7 nm. Silver nanoparticles were dispersed on the N-OLCN with particle sizes ranging from 15 to 20 nm. Zinc nanoparticles were agglomerated onto the surface of the N-OLCN support material. The data indicate that the Ag and the Zn do not disperse well on the N-OLCN surface.

Fig. 1 shows the typical TEM images, EDS maps (obtained from SEM), and particle size distribution of the prepared bimetallic Pd/Ag/N-OLCN and Pd/ZnO/N-OLCN catalysts. As depicted in Fig. 1(a) when Zn ions are added to Pd ions in solution the nanoparticles on the N-OLCN support surface show well-distributed particles with some agglomeration of the metal crystallites. ImageJ software was utilized to evaluate the average particle size from about 70 particles in random regions. The average nanoparticle size of Pd/ZnO was found to be 10.4 ± 1.8 nm. Fig. 1(b) shows that the Pd/Ag nanoparticles are better dispersed on the surface of the N-OLCN support material, but with a wide range of particle sizes and an average size of 16.9 ± 4.8 nm (Fig. 1(f)). EDS mapping displayed in Fig. 1(c and d), corroborated the existence of carbon, oxygen, nitrogen, silver, zinc, and palladium in the bimetallic Pd/ZnO/N-OLCN and Pd/Ag/N-OLCN nanomaterials. This suggests that the Pd affects the ZnO and Ag interaction with the carbon surface.

3.1.2. Thermogravimetric analysis

The TGA data for the N-OLCN, ZnO/N-OLCN, Ag/N-OLCN, Pd/ZnO/N-OLCN, and Pd/Ag–*N*-OLCN nanocatalysts are presented in Fig. 2. The TGA profile of the mono and bimetallic nanomaterials shown in Fig. 2 (a).

A comparison of the TGA data of the N-OLCN with the metal-loaded materials indicates that the ZnO and Ag do not catalyze the carbon oxidation reaction. Also, the derivative peak of the Pd/N-OLCN occurs at ca 680 °C as shown in Fig. S2, also suggesting no carbon catalysis in air. The derivative peaks occur at 645 °C for the monometallic samples. The bimetallic samples show a broad peak at 562 °C and 639 °C for the Pd/ZnO/N-OLCN and the Pd/Ag/N-OLCN electrocatalyst respectively. This is attributed to the oxidation of *N*-OLCN, which occurs at a lower temperature in Pd/ZnO/N-OLCN than it is in Pd/Ag/N-OLCN catalyst. This would suggest that in both these samples two types of metal particles are formed with different carbon oxidation rates. The reason for this observation is not clear at this stage but may relate to particles with different Pd and ZnO (or Ag) concentrations.

The residual weight of both ZnO/N-OLCN and Ag/N-OLCN is 6.2 % and for both Pd/ZnO/N-OLCN and Pd/Ag/N-OLCN is 12.1 % respectively. In addition, the residual weight of the Pd/N-OLCN is 9.8 % which is close to the nominal 10 % Pd loading (see Fig. S2) [30].

3.1.3. X-ray diffraction patterns

Fig. 3 shows the powder XRD patterns for the synthesized Zn/N-OLCN, Ag/N-OLCN, Pd/Zn/N-OLCN, and Pd/Ag/N-OLCN nanomaterials. The XRD peak at 2θ value at ca. 25° for the mono and bimetallic nanomaterials is ascribed to the hexagonal system of the C (002) graphite plane [31]. For comparison, the XRD pattern for Pd/N-OLCN at 40.08°, 46.7°, 68.4°, and 82.0°, assigned to the (111), (200), (220) and (222) planes of palladium facets, are shown in Fig. S2.

The XRD patterns for the Zn/N-OLCN and Pd/Zn/N-OLCN

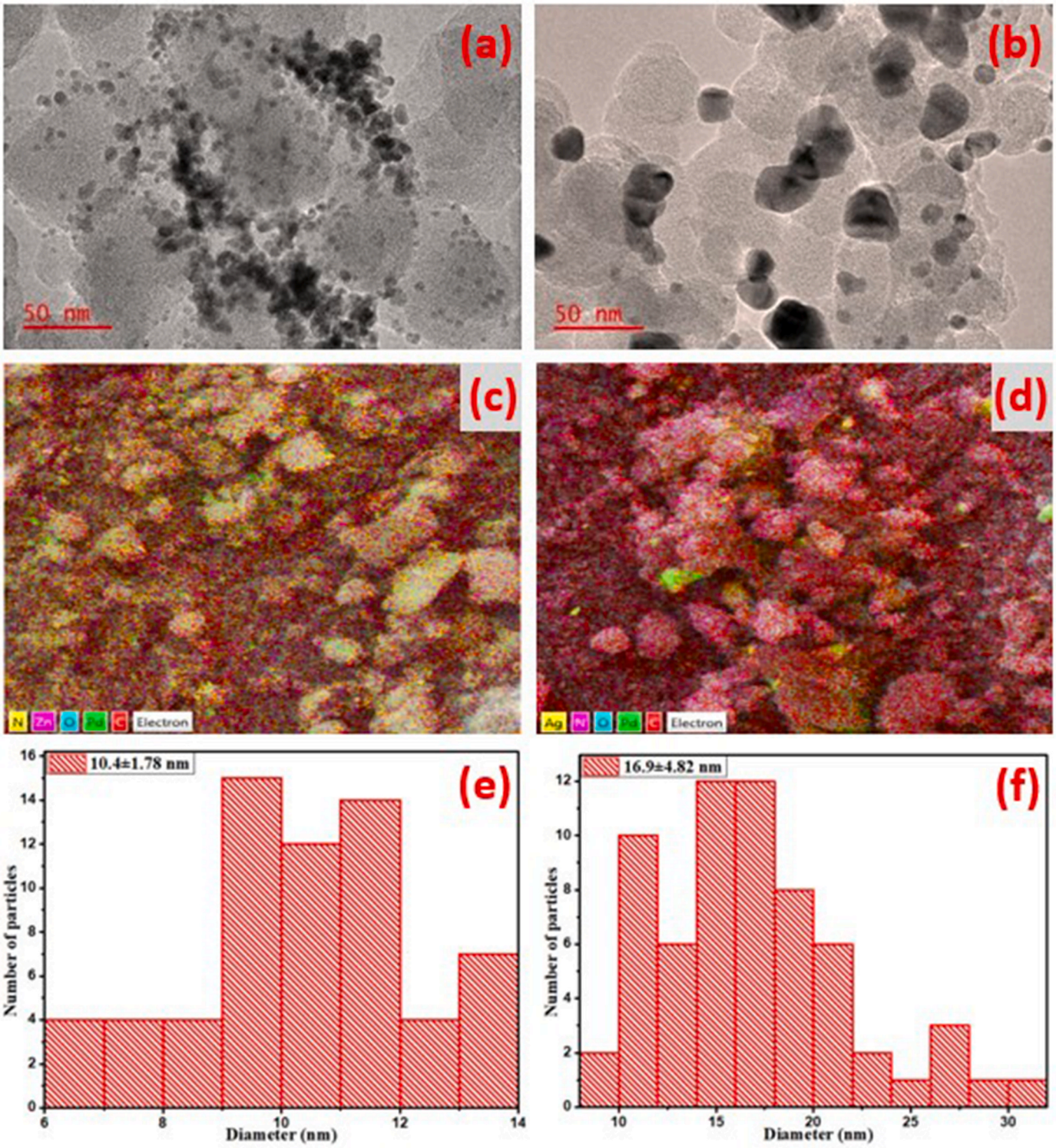

Fig. 1. TEM micrographs, EDS mapping and average particle size of the Pd/Ag/N-OLCN (a, c and e), and the Pd/ZnO/N-OLCN (b, d and f) nanomaterials.

nanomaterials show the presence of Zn and Pd, respectively. The measured peak positions, 2θ, of the Pd/Zn/N-OLCN, Pd/Ag/N-OLCN, and Pd/N-OLCN crystalline planes from (111) to (222) are shown in Table S1. The four diffraction peaks at 2θ = 31.2°, 33.7°, 35.9°, 46.9° and 67.6° were attributed to the wurtzite structure of ZnO while the peaks at 40.4°, 46.9°, 68.6°, and 82.3° corresponds to nanocrystalline Pd metal [15]. When comparing the XRD patterns for Pd in Pd/ZnO/N-OLCN a greater positive shift of the Pd–Zn peaks to higher angle values is observed. This shift is an indication that Zn may be alloyed to palladium [15]. As shown in Fig. 3, the XRD peaks for Ag/N-OLCN at 38.1° and 46.1° correspond to Ag with fcc structure. The peaks for Pd/Ag/N-OLCN at 39.8°, 46.1°, 67.7°, and 81.6° correspond to the Pd crystallographic (111), (200), (220), and (222) planes with the shifts suggesting the formation of a fcc PdAg alloy. For Pd/Ag/N-OLCN the Pd peaks shift to a smaller 2θ angle due to the existence of Ag, suggesting that the Pd is alloyed to Ag metal [32]. The mean particle size of the Pd/Ag/N-OLCN and Pd/ZnO/N-OLCN were determined to be 15.5 nm and 9.8 nm from the Pd (111) peak, using the Debye–Scherrer

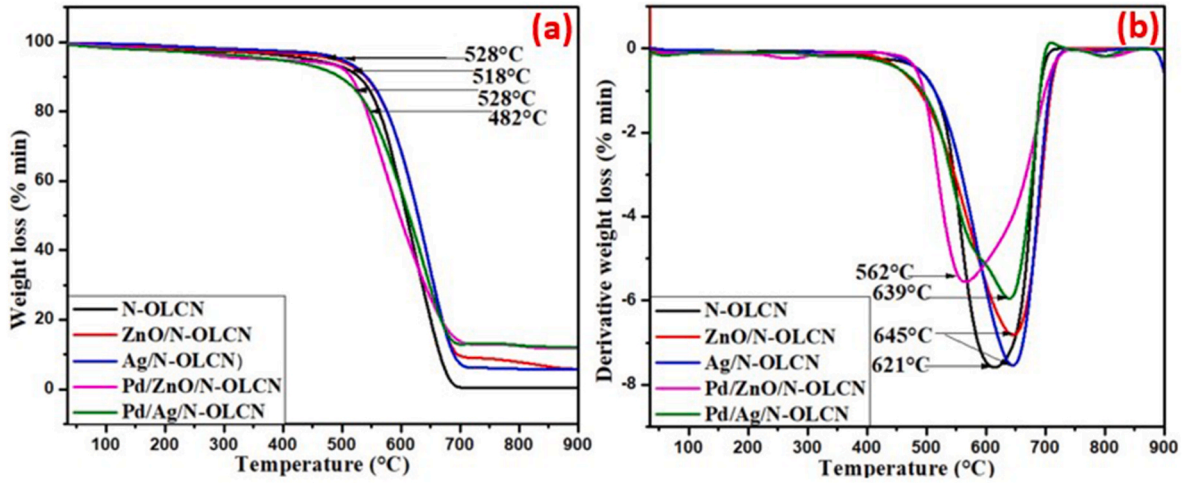

Fig. 2. (a) TGA profile and (b) TGA derivatives of N-OLCN, Zn/N-OLCN, Ag/N-OLCN, Pd/Zn/N-OLCN and Pd/Ag/N-OLCN nanomaterials.

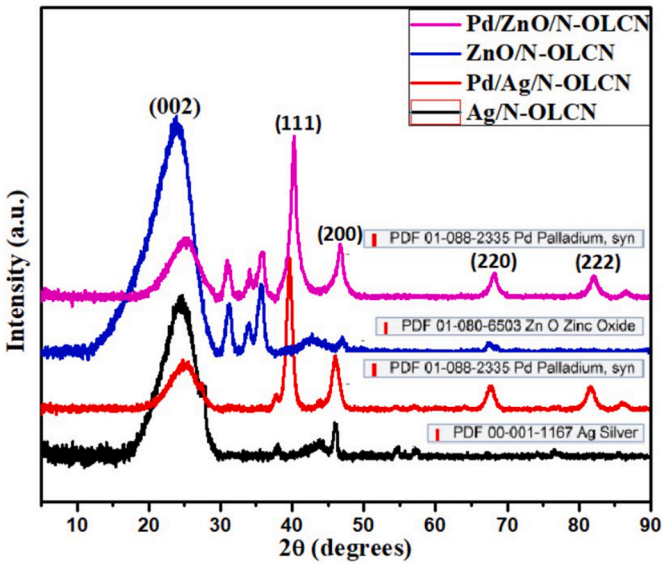

Fig. 3. X-ray diffractograms of Ag/N-OLCN, Pd/Ag/N-OLCN, ZnO/N-OLCN and Pd/ZnO/N-OLCN nanomaterials.

equation respectively. The data measured using TEM micrographs and the XRD data are in excellent agreement. No characteristic peaks from other phases were detected.

3.1.4. *X-ray photoelectron spectroscopy*

XPS measurements were carried out on Pd/ZnO/N-OLCN and Pd/Ag/N-OLCN to determine the oxidation state and surface composition of the palladium bimetallic nanomaterials (Fig. 4). The XPS survey spectra confirmed the presence of C, O, N, Zn, Ag and Pd elements in the two samples (Fig. S4(a)). The elemental composition of the Pd/ZnO/N-OLCN and Pd/Ag/N-OLCN samples is shown in Table 1. The surface % data are similar to that expected from the synthesis procedure used to make the 10 % catalysts (containing 6 % Pd).

Chemical identification and quantification of the constituents of the Pd/ZnO/N-OLCN and Pd/Ag/N-OLCN nanocatalysts are displayed in Table S2. Interestingly, the data (element type/% abundance) for the two materials, after peak deconvolution, are very similar, suggesting that the ZnO or Ag do not modify the support substantially.

Deconvolution of the C 1s spectra of Pd/Zn/N-OLCN (Fig. 4(a)) and Pd/Ag/N-OLCN (see Fig. S4 (b)) was performed and peaks were assigned to (*C*–C) sp^2 (284.2 eV), (*C*–C) sp^3 (284.7 eV), (*C*–O) (285.7 eV), (C═O) (287.1 eV), (*O*–C═O) (288.7 eV) and (*C*–C) sp^2 (284.2 eV), (*C*–C) sp^3 (284.7 eV), (*C*–O) (285.7 eV), (C═O) (287.1 eV) and (*O*–C═O) (288.5 eV), respectively [20]. Fig. 4(b) shows the deconvoluted peaks of the O 1s XPS spectra of Pd/Zn/N-OLCN (organic *C*–O (532.0 eV), organic C═O (533.4 eV), metal oxide (530.5 eV)) and Pd/Ag/N-OLCN (organic *C*–O (531.9 eV), organic C═O (533.3 eV), metal oxide (530.5 eV)) (see Fig. S4(b)) were very similar. The high-resolution N 1s XPS peak of Pd/Zn/N-OLCN is shown Fig. 4(c) and Pd/Ag/N-OLCN (see Fig. S4(b)), were deconvoluted into four peaks that correspond to pyridine-type nitrogen (N-1) (397.5 eV), pyrrole type nitrogen (N-2) (400.3 eV), graphitic type nitrogen (N-3) (402.1 eV), oxidized type nitrogen (N-4) (404.2 eV) and pyridine-type nitrogen (N-1) (398.5 eV), pyrrole type nitrogen (N-2) (400.4 eV), graphitic type nitrogen (N-3) (402.1 eV), and oxidized type nitrogen (N-4) (404.3 eV), respectively [24]. The existence of these nitrogen species in the carbon structure provides abundant electrochemical active catalytic sites for improved interaction and fuel cell behavior [33].

Fig. 4(d) shows the XPS Zn*2p* core level spectra of the Pd/Zn/N-OLCN nanomaterial, which shows two peaks at 1022.5 and 1045.5 eV. These correspond to zinc oxide (Zn $2p_{3/2}$; Zn $2p_{1/2}$), indicating that no Zn (0) is seen in the samples [34]. The high-resolution XPS spectra of the Ag 3d region in the Pd/Ag/N-OLCN nanomaterial shows the two peaks due to Ag $3d_{5/2}$ and Ag $3d_{3/2}$ at 367.4 eV and 373 eV (Fig. 4(e)). It is difficult to assign the peaks to an Ag oxidation state from the data, but together with the XRD data, the Ag peaks are assigned to Ag (0) [35].

The high resolution XPS Pd 3 d spectra for Pd/Zn/N-OLCN are shown in Fig. 4(f). The observed XPS peaks of Pd $3d_{5/2}$ and Pd $3d_{3/2}$ on the Pd/Zn/N-OLCN nanomaterial appeared at 335.2 and 340.4 eV, respectively, which are in good agreement with those reported in the literature [36,37]. These values are characteristics of Pd-species with mixed valences. The XPS peaks appearing at 336.89–337.31 eV and 342.51–344.27 eV BEs on Pd/ZnO/N-OLCN correspond to the surface Pd-species of PdO and $Pd(OH)_2$, respectively [38]. In Fig. S4(b), the Pd/Ag/N-OLCN nanomaterial showed two XPS peaks at 335.1 and 340.5 eV, confirming that the metallic Pd surface contains the Pd^0 and Pd^{2+} species [39].

3.1.5. *Brunauer-Emmett-Teller nitrogen adsorption data*

Nitrogen (N_2) physisorption analysis and the Barrett, Joyner, and Halenda (BJH) technique were used to ascertain the specific surface area (SSA), pore volume, and pore size distribution (PSD) of the N-OLCN, Ag/N-OLCN, ZnO/N-OLCN, Pd/N-OLCN, Pd/Ag/N-OLCN and Pd/ZnO/N-OLCN nanomaterials. Fig. S5 shows the nitrogen adsorption-desorption isotherms and pore size distribution of the synthesized Pd/Ag/N-OLCN and Pd/ZnO/N-OLCN nanomaterials. The BET surface

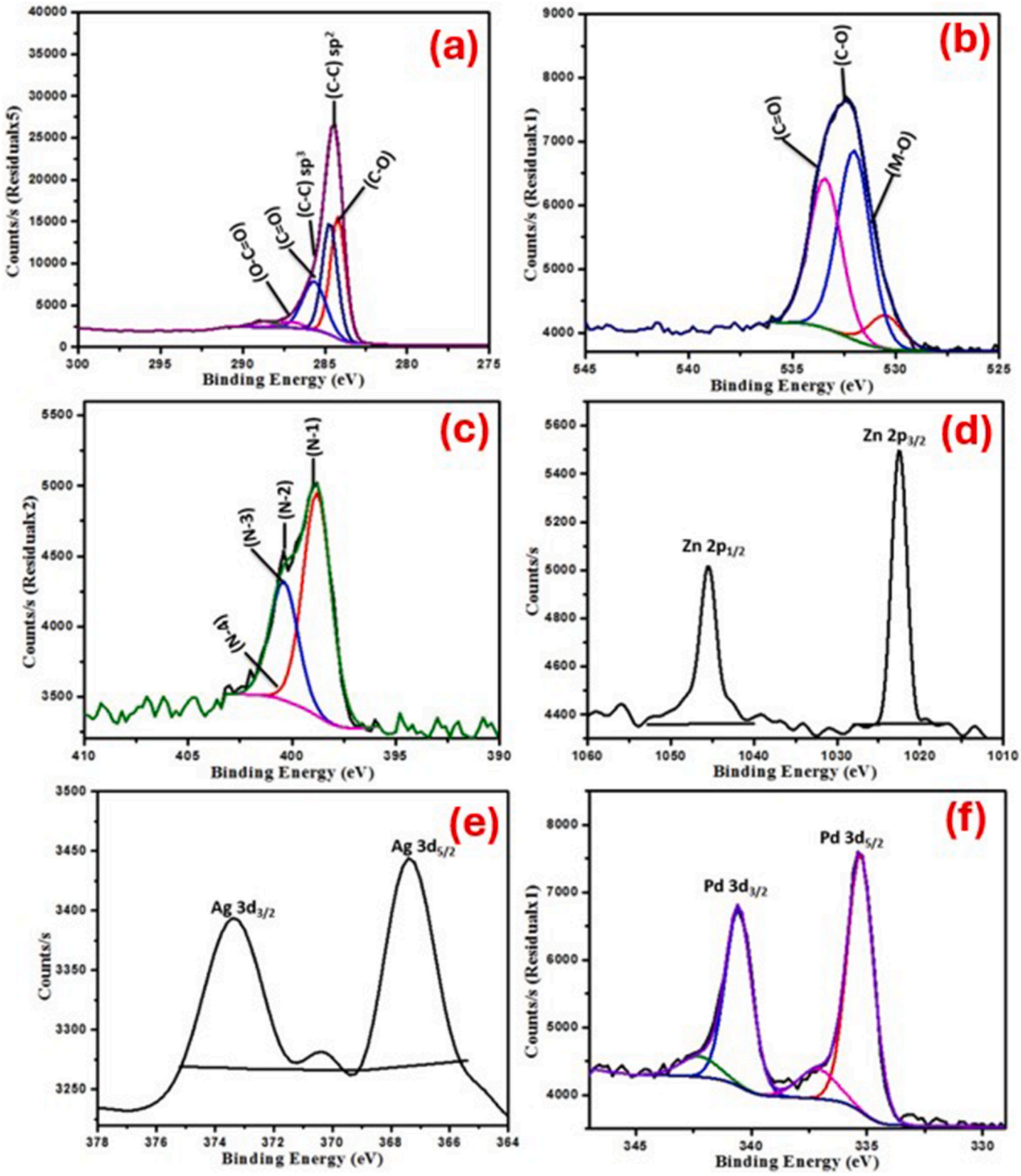

Fig. 4. XPS spectra of Pd/ZnO/N-OLCN for (a) C1s (b), O1s, (c) N1s, (d) Zn2p, (e) Ag3d and (f) Pd3d for Pd/ZnO/N-OLCN nanomaterials.

areas are shown in Table 2. The BET of the support (73.2 m^2 g^{-1}) was reduced substantially on addition of the Ag and Zn (35.3, 24.1 m^2 g^{-1}). Interestingly the Pd-supported catalysts (monometallic/bimetallic) showed a lower surface area reduction (Table 2: 52.6, 62.2, and 68.3 m^2 g^{-1}). The decrease in the BET surface area of the metal-based electrocatalysts is due to the Pd, ZnO, and Ag nanoparticles blocking the surface pores of the N-OLCN support material. The smaller effect of the Pd may be due to (i) the smaller size of the Pd particles (see TEM data above) and/or (ii) the Pd preferentially being attracted to N sites on the support [40]. As presented in the table, bimetallic catalysts typically reveal higher surface areas compared to their monometallic counterparts. This increased surface area results from the unique arrangement of atoms in

Table 1
Elemental composition data obtained from Pd/Zn/N-OLCN and Pd/Ag/N-OLCN XPS data.

Sample	Carbon (wt. %)	Oxygen (wt. %)	Nitrogen (wt. %)	Zinc (wt. %)	Silver (wt. %)	Palladium (wt. %)
Pd/ZnO/N-OLCN	81.8	4.3	3.5	4.4	–	6.1
Pd/Ag/N-OLCN	82.1	4.5	3.3	–	4.2	5.9

Table 2
BET surface area of *N*-OLCN, Ag/N-OLCN, ZnO/N-OLCN, Pd/N-OLCN, Pd/Ag/N-OLCN and Pd/ZnO/N-OLCN nanomaterials.

Nanomaterials	Surface area (m^2g^{-1})	Pore volume (cm^3g^{-1})
N-OLCN	73.2	0.11
Pd/N-OLCN	52.	0.19
Ag/N-OLCN	35.7	0.13
ZnO/N-OLCN	24.1	0.08
Pd/Ag/N-OLCN	62.2	0.14
Pd/ZnO/N-OLCN	68.	0.12

bimetallic structures. Furthermore, the presence of two different metal species allows for more active sites and efficient utilization of the catalyst surface [41].

3.2. Electrocatalytic behavior of the nanocatalysts

3.2.1. Electrochemical surface area

Fig. 5 Shows the cyclic voltammetry (CV) data for the Pd/C, Pd/N-OLCN, Pd/Ag/N-OLCN- and Pd/ZnO/N-OLCN nanocatalysts in an Ag-saturated electrolyte of 1 M NaOH at a scan rate 50 mV s^{-1}. As depicted in Fig. 5(a), the CV curves of all nanocatalysts demonstrate the typical characteristics of palladium-containing nanocatalysts in alkaline conditions [42]. The voltammetric curves show four distinctive potential regions in the anodic scan. Potential region one (QH) (−0.7 V) is attributed to the hydrogen-adsorption peak area, potential region two (−0.6 to −0.3 V) is accredited to the formation of palladium hydroxides Pd(OH), while potential region three and four (−0.3 to 0.4 V) are associated with the oxidation of palladium (and possibly silver and zinc oxide). The palladium oxide reduction peaks for Pd/Ag/N-OLCN and Pd/ZnO/N-OLCN are more prominent as compared to Pd/N-OLCN and Pd/C, suggesting that the nanocatalysts are influenced by the Ag and ZnO. The current values for the Pd electrocatalysts have been normalized by the electrode geometric surface area to give the current density. The ECSA of the four nanocatalysts was calculated by integrating the palladium oxide reduction peak from the CV curves and using equation (1) [43].

$$ECSA_{Pd,cat}\left[m^2g^{-1}\right] = \frac{Q_O[mC]}{Q_{density}[mCcm^{-2}] \times L_{metal}[mg]} \quad (1)$$

where Q_O is the electro-oxidation charge resulting from the integration of the PdO reduction peaks, $Q_{density}$ is the electric reduction charge for an oxygen monolayer on Pd (0.405 mC cm^{-2}) and L_{metal} is the total mass of Pd loaded on the glassy carbon electrode in mg. The ECSA data followed the order: Pd/Zn/N-OLCN (79.24 m^2 g^{-1}) > Pd/Ag/N-OLCN (75.67 m^2 g^{-1}) > Pd/N-OLCN (58.48 m^2 g^{-1}) > Pd/C (53.91 m^2 g^{-1}). The improved ECSA of the Pd/ZnO/N-OLCN and Pd/Ag/N-OLCN can be attributed to the formation of additional active sites at the intersection between Pd and the metal (ZnO and Ag) nanoparticles, improved by the N-OLCNs.

The effect of the catalysts on the CH_3OH reaction was then investigated. Fig. 5(b) compares the cyclic voltammetric curves for the Pd/C, Pd/N-OLCN, Pd/Ag/N-OLCN, and Pd/ZnO/N-OLCN electrocatalysts in 1 M NaOH + 1 M CH_3OH solution at a scan rate of 50 mV s^{-1}.

All CV curves of the electrocatalysts revealed two typical characteristic peak currents for the methanol oxidation reaction (MOR) [44]. A clear anodic current peak in the forward sweep (I_f) and a cathodic current peak in the reverse sweep (I_b) can be detected for all the palladium-based electrocatalysts. In a MOR, the anodic peak current density at the forward sweep (I_f) indicates the dehydrogenation of adsorbed methanol to generate Pd-adsorbed chemisorbed species such as carbon monoxide (CO). This Pd-adsorbed CO can function as an electrocatalyst poison, while the peak current density at the reverse sweep (I_b) is mainly attributed to the oxidation of the adsorbed chemisorbed species [45]. The MOR reactions are:

In forward scan

$$\text{Pd-catalyst} + CH_3OH \rightarrow \text{Pd-catalyst}-(CH_3OH)_{ad} \quad (2)$$

$$\text{Pd-catalyst}-(CH_3OH)_{ad} \rightarrow \text{Pd catalyst} - (CO) + 4H^+ + 4\,e^- \quad (3)$$

$$\text{Pd-catalyst} + H_2O \rightarrow \text{Pd-catalyst}-(OH)_{ad} + H^+ + e^- \quad (4)$$

In reverse scan

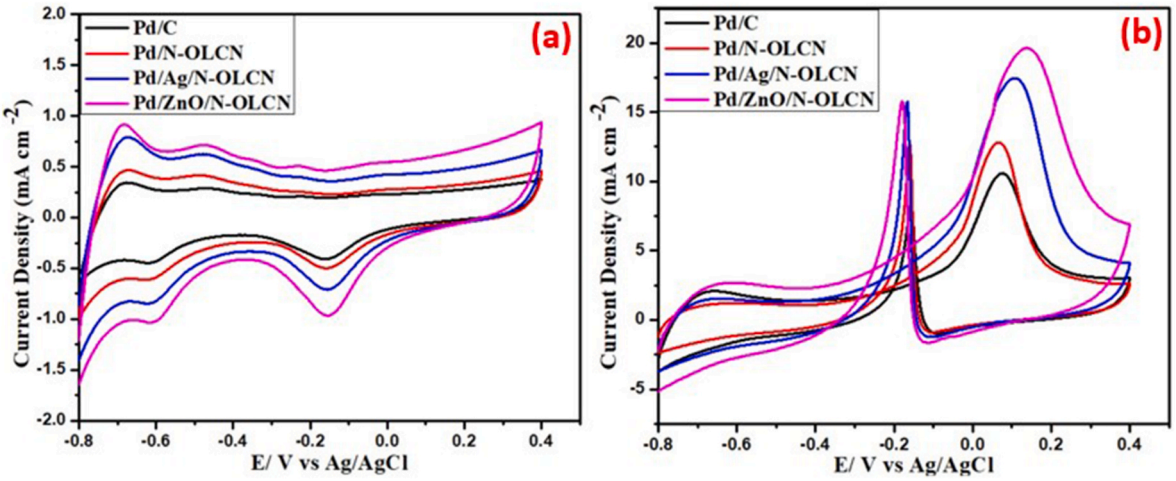

Fig. 5. CV curves of Pd/C, Pd/N-OLCN, Pd/Ag/N-OLCN, and Pd/ZnO/N-OLCN modified electrodes (a) in 1 M NaOH solution at scan rate 50 mV s^{-1} (b) in 1 M NaOH + 1 M CH_3OH solution at a scan rate of 50 mV s^{-1}.

$$\text{Pd-catalyst}-(\text{CO})_{ad} + \text{Pd-catalyst}-(\text{OH})_{ad} \rightarrow \text{Pd-catalyst} + \text{CO}_2 + \text{H} + \text{e}^- \quad (5)$$

The catalytic activity shown by the cyclic voltammograms of the synthesized electrocatalysts towards the methanol oxidation reactions (MOR) can be discussed in terms of three parameters: (1) the forward anodic peak current, (2) the onset oxidation potential and (3) CO tolerance [46]. As shown in Fig. 5(b), the Pd/ZnO/N-OLCN (19.7 mA cm^{-2}) displayed a higher peak current density and hence the best activity as compared to the Pd/Ag/N-OLCN (17.6 mA cm^{-2}), Pd/N-OLCN (12.8 mA cm^{-2}), and a commercial Pd/C (10.5 mA cm^{-2}) electrocatalyst for MOR, in alkaline media. The addition of ZnO and Ag to the Pd/N-OLCN significantly enhanced the catalytic activity towards MOR in an alkaline electrolyte. This might be ascribed to the nitrogen-doped onion-like carbon nanoparticles which produce a strong interlinkage between Pd and (ZnO and Ag) nanoparticles resulting in a high electronic conduction and good metal nanoparticle dispersion. Furthermore, the improved catalytic activity of the electrocatalysts towards MOR can be ascribed to its higher pyrrolic-N, pyridinic-N content, and mesoporous structure of N-OLCN, which gives a high density of anchoring sites and mass diffusion enhancement for MOR [47]. Pyrrolic-N sites are known to facilitate the adsorption of reactants and intermediate species during MOR, promoting efficient electron transfer and reaction pathways. Pyridinic-N contributes to the overall basic sites of the material and these sites are essential for MOR because they assist in breaking the *C*–H bond in methanol, leading to the desired oxidation reaction [47]. Pyridinic-N sites enhance the overall reactivity of the catalyst, making it more effective in MOR.

Interestingly, the smaller sized particle of the Pd/ZnO/N-OLCN electrocatalyst, observed by TEM, suggests that the increased catalytic activity of this electrocatalyst is related to its larger BET-specific surface area and electrochemical active surface area as compared to the Pd/Ag/N-OLCN electrocatalyst [48]. Smaller particle size leads to more active sites, allowing for better interaction with reactants and intermediates during the methanol oxidation process. Furthermore, when metal oxides are doped into the catalyst, they enhance its catalytic activity. These oxides can act as promoters, improving the kinetics of reactions occurring at the electrode surfaces. In contrast, alloy catalysts may not exhibit the same level of catalytic activity. While some alloy materials are effective, they may not always surpass the performance of metal oxide-doped catalysts [49]. The onset potential for Pd/ZnO/N-OLCN (−0.32 V) showed the most negative value (compared with Pd/Ag/N-OLCN (−0.29 V), Pd/N-OLCN (−0.27 V), and Pd/C (−0.26 V)). This is proposed to be due to the bifunctional complex. Zn is an oxophilic element that has an oxygen adsorbing character which releases the carbonaceous intermediate species and assists the methanol electrooxidation leading to a more negative onset oxidation potential and improved catalytic performance [50]. In ZnO semiconductor, the electron (e^-) can be conducted from its valence band (VB) to the conduction band (CB) at low overpotentials. The outcome of this phenomenon is the formation of holes in VB (h^+) that will act as oxidizing sites. In h^+ of the ZnO surface, water (H_2O) acts as an electron donor and generates OH°. Hydroxyl radicals can oxidize COads and prevent Pt or Pd active sites from poisoning [51].

Also, the existence of Ag metal can promote the electrooxidation of reaction chemisorbed species, especially carbon monoxide adsorption. As a result, alloying Pd with Ag hinders the poisoning of the active Pd sites, such as CO intermediates, and enhances the electrocatalytic activity [52]. The promoting effect of the second metal has been explained by a bi-functional mechanism and electronic (ligand) effects [53]. According to the d-band theory of Nørskov and co-workers, after the combination of Ag with Pd, the d-band center of Pd may be shifted up [54,55]. In other words, the second metal can promote methanol oxidation by changing the electronic properties of Pd. Additionally, in the bi-functional mechanism, the second metal activates water at lower potentials than Pt or Pd and the activated water can oxidize the adsorbed CO or other poisoning intermediate and therefore liberate Pt or Pd active sites [56]. The ratio of the forward current oxidation peak (I_f) to the reversed current oxidation peak (I_b) is used to measure the poison tolerance from carbonaceous species accumulation on Pd-based electrocatalysts towards MOR [57]. The I_f/I_b ratio of the forward and backward currents is 1.3 for Pd/ZnO/N-OLCN, 1.1 for Pd/Ag/N-OLCN, 1.0 for Pd/N-OLCN, and 0.9 for Pd/C. A high I_f/I_b ratio demonstrates efficient methanol oxidation during the forward sweep and the formation of only a small accumulation of carbonaceous intermediates. Table 3 presents a comparison of the new electrocatalysts used for the methanol oxidation reactions, in terms of current density, with other Pd/C catalysts that are similar. It is noteworthy that our prepared electrocatalysts in general reveal similar electrocatalytic performance towards methanol oxidation reactions (MOR) compared to the other catalysts listed.

3.2.2. The effect of scan rate (SR) on the current density

The Pd/Ag/N-OLCN and Pd/ZnO/N-OLCN electrocatalysts had a better low onset oxidation potential, poison tolerance towards carbonaceous intermediates, and higher peak current densities, than the Pd/N-OLCN and Pd/C electrocatalysts. Fig. 6 indicates distinctive CVs for the Pd/Ag/N-OLCN and Pd/ZnO/N-OLCN in the presence of 1 M NaOH +1 M CH_3OH solution. As displayed in Fig. 6(a) and (b), the catalytic activity for both bimetallic electrocatalysts increased with the positive shift of the anodic oxidation peak current as the scan rate increased from 10 mV s^{-1} to 100 mV s^{-1} which may be ascribed to fast electron flow at the interface of the electrolyte/electrode. A plot of the anodic current density and the square root of the sweep rate investigated are shown in Fig. 6(c) and (d). The anodic peak current density is seen to be linearly associated with the square root of the scan rates, demonstrating a typical diffusion-controlled reaction kinetics [61]. Clearly, the higher the slope, the faster the electron transfer rate. As the SR increases, improving methanol kinetic oxidation is referred to as "enhancing oxidation current density". The potential's square root determines how tall the peak is. Consequently, as opposed to the reversible state, the anodic–cathodic peak separation becomes greater. The greatest current density belongs to Pd/ZnO/N-OLCN at 0.4 E/V potential compared with Pd/Ag/N-OLCN. This reflects the synergistic effect of ZnO on Pd/ZnO/N-OLCN catalytic activity.

3.2.3. Chronoamperometry

CA tests were done to study the electrocatalytic stability of the Pd/C, Pd/N-OLCN, Pd/Ag/N-OLCN, and Pd/ZnO/N-OLCN electrocatalysts in the methanol oxidation reaction in alkaline conditions at an applied potential of −0.30 V. Fig. 7(a) displays the behavior of the peak current density as a function of time. Stability studies were carried out for all the Pd-based electrocatalysts in 1 M NaOH +1 M CH_3OH solution for a period of 2000 s. As shown in Fig. 7(a) the current densities for the Pd/C, Pd/N-OLCN, Pd/Ag/N-OLCN, and Pd/ZnO/N-OLCN electrocatalysts decayed rapidly initially, mainly because of the formation of poisoning chemisorbed species like CO_{ad} on the Pd active sites, and then slowly stabilized. It can be observed that the Pd/ZnO/N-OLCN (4.1 mA cm^{-2}) electrocatalyst produced a higher potentiostatic current density followed by Pd/Ag/N-OLCN (3.6 mA cm^{-2}), Pd/N-OLCN (3.0 mA cm^{-2}) and Pd/C (2.5 mA cm^{-2}), indicating that this electrocatalyst was the

Table 3
Comparison of Pd/N-OLCN, Pd/Ag/N-OLCN, and Pd/ZnO/N-OLCN to other Pd/C catalysts reported for MOR.

Electrocatalysts	Fuel (M)	Electrolyte (M)	CD (mA cm^{-2})	Ref.
Pd/ZnO/N-OLCN	1 CH_3OH	1 NaOH	19.7	This work
Pd/Ag/N-OLCN	1 CH_3OH	1 NaOH	17.6	This work
Pd/N-OLCN	1 CH_3OH	1 NaOH	12.9	This work
Pd/Zn/N–C	1C_2H_5OH	1 KOH	18.1	[58]
Pd/Ag/C	0.5 CH_3OH	1KOH	15.8	[59]
Pd/Fe/GCN	0.5C_2H_5OH	0.5 KOH	17.4	[60]
Pd/CO/N-G	1 CH_3OH	1 KOH	21.3	[33]

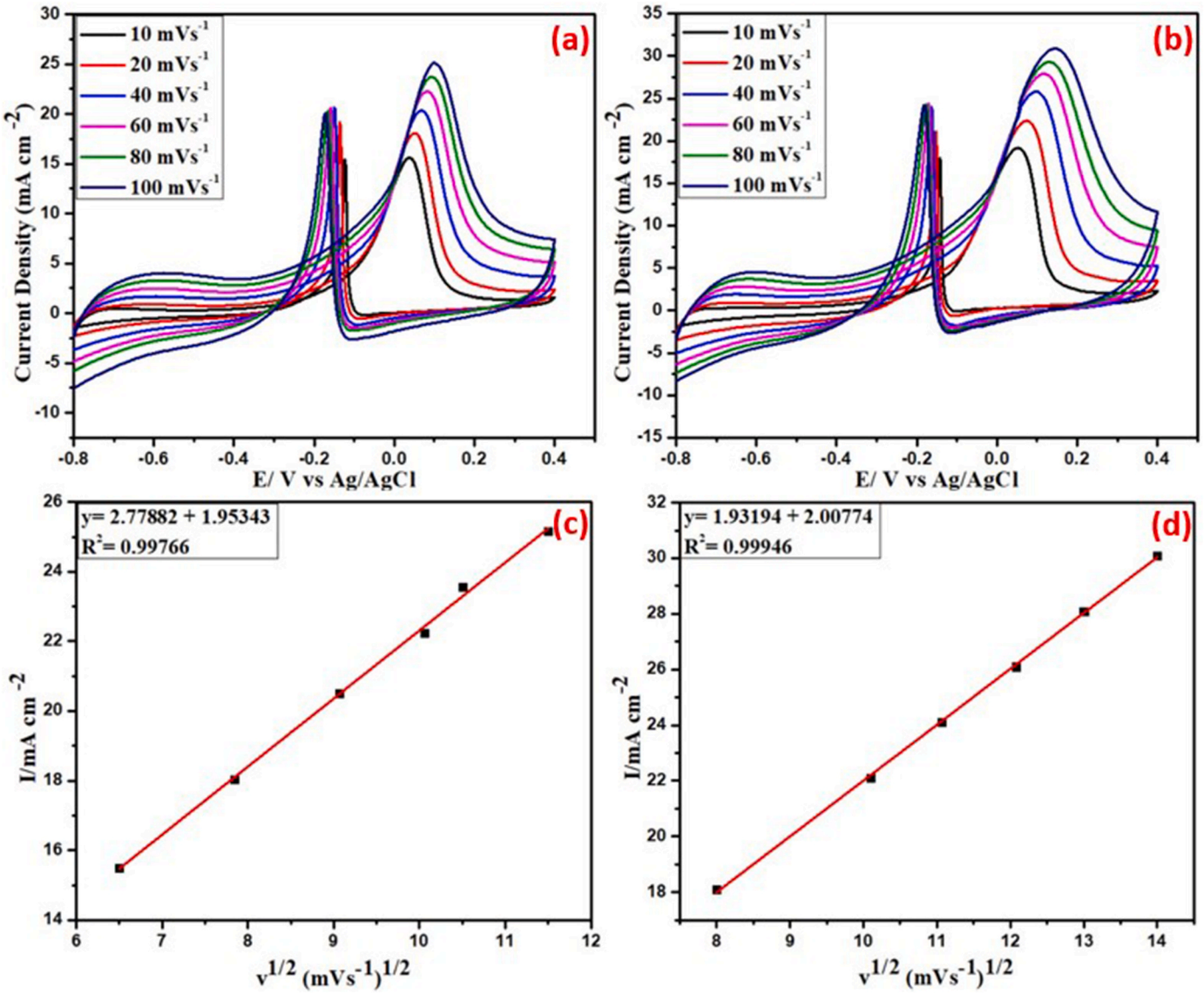

Fig. 6. CV curves for the Pd/Ag/N-OLCN and Pd/ZnO/N-OLCN electrocatalysts in 1 M NaOH +1 M CH_3OH at different scan rates [(a) and (b)] and the plots of peak current density vs. square root of scan rates [(c) and (d)].

most stable in the MOR in alkaline media. Metal oxides can stabilize the catalyst structure, preventing agglomeration and maintaining long-term stability. While alloy catalysts can suffer from phase separation or dissolution over time, leading to reduced stability [49]. Chronoamperometry measurements confirmed that the bimetallic electrocatalysts had better steady-state catalytic performance as compared to the monometallic electrocatalysts. This enhancement in electrocatalytic stability was associated with the influence of the ZnO and Ag nanoparticles on the N-OLCN surface as observed by XRD and CV studies [39, 58].

For a correlation to CO poisoning, the poisoning rate σ (% s^{-1}) for CA curves was calculated utilizing the most linear part of the curve using the following formula:

$$\sigma = \frac{100}{I_0}\left(\frac{dI}{dt}\right)_{t>400s} \quad (6)$$

where $\left(\frac{dI}{dt}\right)_{t>400s}$ is the slope of the linear portion of CA, t is time in seconds, and I_0 is the back extrapolated current density % at the point of linear CA portion. The calculation procedure was proposed by Jiang et al. [62] for MOR on PtRu electrocatalysts. The same procedure was adopted by Guo et al. [63] for MOR. The calculated values for σ (%s^{-1}) are in the following order Pd/ZnO/N-OLCN < Pd/C < Pd/N-OLCN < Pd/Ag/N-OLCN as illustrated in Table 4. This shows that Pd/ZnO/N-OLCN had the lowest poisoning rate and hence higher tolerance to poisonous intermediates formed during MOR than the other electrocatalysts and the commercial Pd/C. The contribution of ZnO and the hybrid support system are visualized in the σ (%s^{-1}) values as the realized reduction in poisoning rates for Pd or Pd/ZnO NPs supported on N-OLCN. Thus, synergy-coupled heteroatom doping, unifying the Pd NPs with the hybrid support system is important in CO poisoning tolerance, stability, and durability.

The low poisoning rate for Pd/ZnO/N-OLCN is attributed to the strong support metal interaction (SMSI) and synergistic effects arising between Pd NPs with ZnO NPs, Ag, and/or N-OLCN, and the higher ECSA observed for Pd/ZnO/N-OLCN ensuring exposure of active sites, which was also in good agreement with the CV measurements.

Apart from Chronoamperometry stability, accelerated CV cyclization was conducted to assess the durability of the electrocatalysts. The curves for relative mass activity current loss (%) versus cycle number from CV sweep cycle studies were used to assess the electrocatalyst durability and

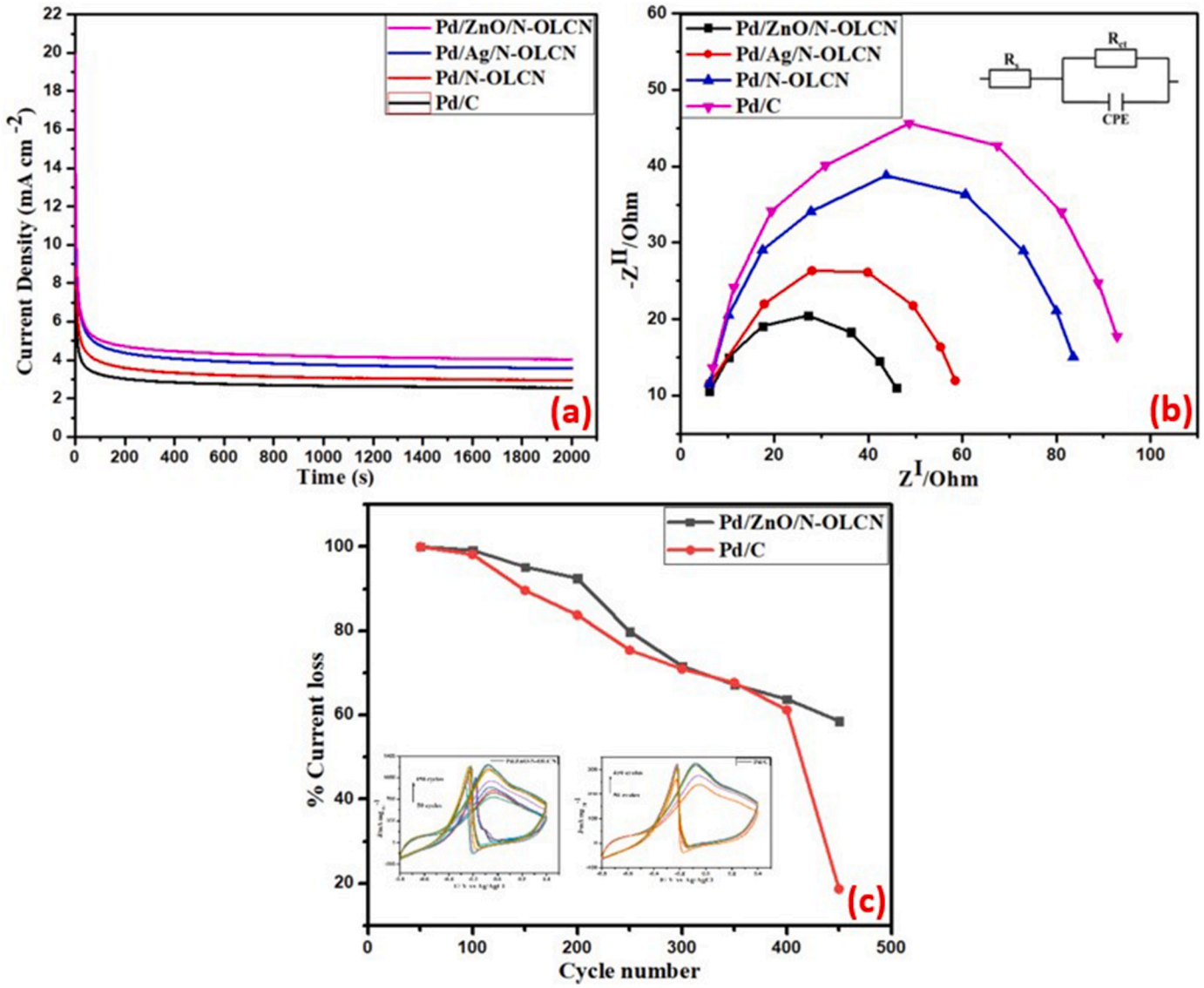

Fig. 7. Chronoamperometric curves and Nyquist plots for Pd/C, Pd/N-OLCN, Pd/Ag/N-OLCN and Pd/ZnO/N-OLCN modified electrodes (a) in 1 M NaOH + 1 M CH_3OH for an applied potential of −0.30 V and (b) in 1 M NaOH + 1 M CH_3OH and the equivalent circuit diagram (insert) and (c) accelerated durability tests performed by CVs continuous cyclization in N_2-saturated 1 M NaOH + 1 M CH_3OH solution for 450 cycles at 50 mVs^{-1}.

Table 4
Summarized electrochemical parameters derived from several electrochemical methods.

Electrocatalysts	*ECSA (m2/g)*	I_f/I_b	R_s *(Ohm)*	R_{ct} *(Ohm)*	*CPE (μF)*	$\sigma(\%\ s^{-1})$
Pd/C	53.91	0.9	45.6	92.8	194.1	0.001447
Pd/N-OLCN	58.48	1.0	38.7	83.3	140.9	0.001446
Pd/Ag/N-OLCN	75.67	1.1	26.2	58.5	189.7	0.002224
Pd/ZnO/N-OLCN	79.24	1.3	20.6	45.8	179.2	0.000124

the calculation of the deactivation rate [64]. After 450 cycles, as shown in Fig. 7 (c), the oxidation peak current densities were 1280 and 324 mA mg_{Pd}^{-1} for the Pd/ZnO/N-OLCN and Pd/C electrocatalysts, respectively, signifying losses of 58.3 % and 17.8 % in the mass activity. The results demonstrated that the Pd/ZnO/N-OLCN catalyst with abundant active planes of ZnO contributed to improved stability and stronger tolerance of CO_{ads} in the MOR process. As seen in the insert for Pd/ZnO/N-OLCN in Fig. 7(c), an interesting phenomenon was observed, where the backward peak shifted to low potential as potential cycles increased (above 150 cycles); we postulate that this can be a change in the exposed electrocatalyst active site and new intermediates all together being oxidized at a different potential.

3.2.4. Electrochemical impedance spectroscopy

The EIS investigations were utilized to compare the reaction process of methanol oxidation on the Pd/C, Pd/N-OLCN, Pd/Ag/N-OLCN, and Pd/ZnO/N-OLCN modified electrodes. The Nyquist impedance for all electrocatalysts in the electrolyte 1 M NaOH containing 1 M CH_3OH solution in the frequency range from 1000 kHz to 0.005 Hz is presented in Fig. 7(b). The EIS experimental data were fitted using the electrical equivalent circuit inserted in Fig. 7(b). The Rs-solution resistance, Rct-charge transfer resistance, and the CPE-constant phase element are associated with the double-layer capacitor of the electrode [65]. The radius of the semicircle was used to estimate the charge transfer resistance of the electrocatalysts at the interface between the electrode and the electrolyte [66,67]. The relevant parameters (solution resistance (Rs), charge transfer resistance (RCT), and constant phase element (CPE) are summarized in Table 4. A smaller impedance arc diameter demonstrates a smaller charge transfer resistance and a higher electrocatalytic

activity for the methanol oxidation reaction [68]. In support of the other electrocatalytic studies, the corresponding Rct of Pd/ZnO/N-OLCN is smaller as compared to Pd/Ag/N-OLCN, Pd/N-OLCN, and Pd/C, indicating that Pd/ZnO/N-OLCN catalysts displayed the smallest electron transfer resistance relative to the other catalysts. When ZnO interacts with other metals, electronic metal-support interactions occur. ZnO has a lower work function compared to other metals. As a result, electrons tend to transfer from ZnO to the metal species. The resulting electron-rich interface enhances the adsorption of oxygen and facilitates the CO oxidation reaction [69]. Also, ZnO can produce hydroxyl radicals and oxidize the intermediate carbonaceous species on the Pd catalyst surface. Likewise, ZnO increased the electrical conductivity which improved the catalytic activity of Pt or Pd [51]. The faster charge transfer resistance at the interface between the electrode and the electrolyte suggests that the electrocatalysts had better electrode dynamics [70]. These outcomes are consistent with the excellent electrocatalytic performance revealed by the CV and CA studies.

4. Conclusions

In summary, nitrogen-doped onion-like carbon nanoparticles (N-OLCNs) have been synthesized via a flame pyrolysis method using acetonitrile as a starting material. The dispersed Pd/Ag and Pd/ZnO nanoparticles supported on the N-OLCNs were successfully synthesized using the sodium borohydride reduction method. The TEM results confirmed the smaller particle size and better dispersion of the Pd/ZnO particles as compared to the larger Pd/Ag nanoparticles on the N-OLCN surface. The most notable difference in the XRD observations between the Pd/ZnO/N-OLCN and Pd/Ag/N-OLCN catalysts is the degree of peak shifting. The Pd peaks in Pd–ZnO peaks shift to higher angle values whereas Pd–Ag peaks shift to a smaller 2θ angle because both ZnO and Ag may be highly alloyed to the Pd structure. The incorporation of Ag and Zn modified the electronic structure of Pd, which was affirmed by the downward shift of the d-band center on Pd using XPS analysis. Among the four nanocatalysts, Pd/ZnO/N-OLCN and Pd/Ag/N-OLCN revealed the highest peak current densities, the most negative onset potentials, and excellent CO-tolerance when compared to the other nanocatalysts in the methanol oxidation reaction in alkaline media. Furthermore, the stability studies carried out using chronoamperometry revealed that Pd/ZnO/N-OLCN and Pd/Ag/N-OLCN nanocatalysts were more stable in MOR as compared to Pd/N-OLCN and commercial Pd/C nanocatalysts. Moreover, Pd/ZnO/N-OLCN and Pd/Ag/N-OLCN both showed a very fast charge transfer rate in MOR as shown in the EIS test. The encouraging catalytic performance demonstrates that the Pd/ZnO/N-OLCN and Pd/Ag/N-OLCN can be promising electrocatalysts for methanol oxidation in fuel cells.

CRediT authorship contribution statement

Ludwe L. Sikeyi: Writing – original draft, Validation, Methodology, Investigation. **Themba D. Ntuli:** Software, Data curation. **Nobanathi W. Maxakato:** Resources, Supervision. **Neil J. Coville:** Resources, Supervision, Writing – review & editing. **Manoko S. Maubane-Nkadimeng:** Conceptualization, Funding acquisition, Project administration, Resources, Supervision, Writing – review & editing.

Declaration of competing interest

The authors declare that they have no known competing financial interests or personal relationships that could have appeared to influence the work reported in this paper.

Data availability

Additional data is provided in Supplementary Information.

Acknowledgments

This work is based on the research supported in part by the National Research Foundation (NRF) of South Africa (Grant Numbers: 118137, 118148), the University of the Witwatersrand (Postgraduate Merit Award, University Research Council), and an NRF-DAAD grant (Grant number: 117841). The authors also acknowledge the efforts and support provided by the University of Johannesburg (Faculty of Science, University Research Council and Centre for Nanomaterials Science Research). Our gratitude goes to Mr Thabo Matthews from the University of Johannesburg (Doornfontein) for the stability data acquisition. We also wish to acknowledge Mr. Siyasanga Mpelane at the University of Johannesburg (Auckland Park) for the high-magnification TEM data.

Appendix A. Supplementary data

Supplementary data to this article can be found online at https://doi.org/10.1016/j.jpowsour.2024.234802.

References

[1] X. Pan, T. Shao, X. Zheng, Y. Zhang, X. Ma, Q. Zhang, Energy and sustainable development nexus: a review, Energy Strategy Rev. 47 (2023) 101078, https://doi.org/10.1016/j.esr.2023.101078.
[2] J.L. Holechek, H.M.E. Geli, M.N. Sawalhah, R. Valdez, A global assessment: can renewable energy replace fossil fuels by 2050? Sustainability 14 (2022) 4792, https://doi.org/10.3390/su14084792.
[3] Z. Pu, G. Zhang, A. Hassanpour, D. Zheng, S. Wang, S. Liao, Z. Chen, S. Sun, Regenerative fuel cells: recent progress, challenges, perspectives and their applications for space energy system, Appl. Energy 283 (2021) 116376, https://doi.org/10.1016/j.apenergy.2020.116376.
[4] V. Cigolotti, M. Genovese, P. Fragiacomo, Comprehensive review on fuel cell technology for stationary applications as sustainable and efficient poly-generation energy systems, Energies 14 (2021) 4963, https://doi.org/10.3390/en14164963.
[5] H. Tian, Y. Yu, Q. Wang, J. Li, P. Rao, R. Li, Y. Du, C. Jia, J. Luo, P. Deng, Y. Shen, X. Tian, Recent advances in two-dimensional Pt based electrocatalysts for methanol oxidation reaction, Int. J. Hydrogen Energy 46 (2021) 31202–31215, https://doi.org/10.1016/j.ijhydene.2021.07.006.
[6] M. Huang, J. Zhang, C. Wu, L. Guan, Networks of connected Pt nanoparticles supported on carbon nanotubes as superior catalysts for methanol electrooxidation, J. Power Sources 342 (2017) 273–278, https://doi.org/10.1016/j.jpowsour.2016.12.054.
[7] R.N. Singh, A. Singh, Anindita, Electrocatalytic activities of binary and ternary composite electrodes of Pd, nanocarbon and Ni for electro-oxidation of methanol in alkaline medium, J. Solid State Electrochem. 13 (2009) 1259–1265, https://doi.org/10.1007/s10008-008-0660-x.
[8] M. Mayilvel Dinesh, T. Huang, S. Yao, G. Sun, S. Mao, Hafnium sulphide-carbon nanotube composite as Pt support and active site-enriched catalyst for high performance methanol and ethanol oxidations in alkaline electrolytes, J. Power Sources 410–411 (2019) 204–212, https://doi.org/10.1016/j.jpowsour.2018.11.021.
[9] H. Liu, D. Yang, Y. Bao, X. Yu, L. Feng, One-step efficiently coupling ultrafine Pt–Ni2P nanoparticles as robust catalysts for methanol and ethanol electro-oxidation in fuel cells reaction, J. Power Sources 434 (2019), https://doi.org/10.1016/j.jpowsour.2019.226754.
[10] Z. Yang, Y. Shi, X. Wang, G. Zhang, P. Cui, Boron as a superior activator for Pt anode catalyst in direct alcohol fuel cell, J. Power Sources 431 (2019) 125–134, https://doi.org/10.1016/j.jpowsour.2019.05.052.
[11] W.A. Auriyani, D. Bustan, S. Haryati, The electrolyte-fuel concentrations effects on direct methanol alkaline fuel cell (DMAFC) through non-noble metal catalysts, Journal of Science and Applicative Technology 5 (2021) 25, https://doi.org/10.35472/jsat.v5i1.388.
[12] L. Zhao, Z.B. Wang, J. Liu, J.J. Zhang, X.L. Sui, L.M. Zhang, D.M. Gu, Facile one-pot synthesis of Pt/graphene-TiO2 hybrid catalyst with enhanced methanol electrooxidation performance, J. Power Sources 279 (2015) 210–217, https://doi.org/10.1016/j.jpowsour.2015.01.023.
[13] Y. Yang, S. Yu, L. Gao, X. Wang, S. Yan, The properties of PdRu/C with respect to the electro-oxidation of methanol and ethanol, Int. J. Electrochem. Sci. 14 (2019) 1270–1282, https://doi.org/10.20964/2019.02.50.
[14] V.F. Ruiz-Ruiz, R. González-Olvera, R. Díaz-Pardo, I. Betancourt, I. Zumeta-Dubé, D. Díaz, N. Farfán, M.J. Arellano-Jiménez, Mechanochemically obtained Pd–Ag nanoalloys. Structural considerations and catalytic activity, Materialia (Oxf) 4 (2018) 166–174, https://doi.org/10.1016/j.mtla.2018.09.031.
[15] X.L. Liang, X. Dong, G.D. Lin, H. Bin Zhang, Carbon nanotube-supported Pd-ZnO catalyst for hydrogenation of CO2 to methanol, Appl. Catal., B 88 (2009) 315–322, https://doi.org/10.1016/j.apcatb.2008.11.018.
[16] H. You, S. Yang, B. Ding, H. Yang, Synthesis of colloidal metal and metal alloy nanoparticles for electrochemical energy applications, Chem. Soc. Rev. 42 (2013) 2880–2904, https://doi.org/10.1039/c2cs35319a.

[17] L. Zhang, Q. Chang, H. Chen, M. Shao, Recent advances in palladium-based electrocatalysts for fuel cell reactions and hydrogen evolution reaction, Nano Energy 29 (2016) 198–219, https://doi.org/10.1016/j.nanoen.2016.02.044.
[18] Y. Wang, Z.M. Sheng, H. Yang, S.P. Jiang, C.M. Li, Electrocatalysis of carbon black- or activated carbon nanotubes-supported Pd-Ag towards methanol oxidation in alkaline media, Int. J. Hydrogen Energy 35 (2010) 10087–10093, https://doi.org/10.1016/j.ijhydene.2010.07.172.
[19] N.T. Kien, K. Hashisake, M. Chiku, E. Higuchi, H. Inoue, Activity and durability of intermetallic PdZn electrocatalyst for ethanol oxidation reaction, Res. Chem. Intermed. 48 (2022) 3795–3810, https://doi.org/10.1007/s11164-022-04780-z.
[20] Y. Zhang, A. Reed, D.Y. Kim, Nitrogen doped carbon nano-onions as efficient and robust electrocatalysts for oxygen reduction reactions, Curr. Appl. Phys. 18 (2018) 417–423, https://doi.org/10.1016/j.cap.2018.02.001.
[21] A. Zhang, Z. Zheng, F. Cheng, Z. Tao, J. Chen, Preparation of Li4Ti5O12 submicrospheres and their application as anode materials of rechargeable lithium-ion batteries, Sci China Chem 54 (2011) 936–940, https://doi.org/10.1007/s11426-011-4296-9.
[22] D. Mohapatra, G. Dhakal, M.S. Sayed, B. Subramanya, J. Shim, S. Parida, Sulfur doping : unique strategy to improve the supercapacitive performance of carbon nano-onions, ACS Appl. Mater. Interfaces 11 (2019) 8040–8050, https://doi.org/10.1021/acsami.8b21534.
[23] M. Zeiger, N. Jäckel, V.N. Mochalin, V. Presser, Review: carbon onions for electrochemical energy storage, J Mater Chem A Mater 4 (2016) 3172–3196, https://doi.org/10.1039/c5ta08295a.
[24] D. Mohapatra, N.S.K. Gowthaman, M.S. Sayed, J.J. Shim, Simultaneous ultrasensitive determination of dihydroxybenzene isomers using GC electrodes modified with nitrogen-doped carbon nano-onions, Sensor. Actuator. B Chem. 304 (2020) 127325, https://doi.org/10.1016/j.snb.2019.127325.
[25] T.H. Mongwe, N.J. Coville, M.S. Maubane-Nkadimeng, Synthesis of Onion-like Carbon Nanoparticles by Flame Pyrolysis, 2022, pp. 198–220, https://doi.org/10.1039/9781839167218-00198.
[26] O. Ornelas, J.M. Sieben, R. Ruiz-Rosas, E. Morallón, D. Cazorla-Amorós, J. Geng, N. Soin, E. Siores, B.F.G. Johnson, On the origin of the high capacitance of nitrogen-containing carbon nanotubes in acidic and alkaline electrolytes, Chem. Commun. 50 (2014) 11343–11346, https://doi.org/10.1039/c4cc04876h.
[27] G. Wu, A. Santandreu, W. Kellogg, S. Gupta, O. Ogoke, H. Zhang, H.L. Wang, L. Dai, Carbon nanocomposite catalysts for oxygen reduction and evolution reactions: from nitrogen doping to transition-metal addition, Nano Energy 29 (2016) 83–110, https://doi.org/10.1016/j.nanoen.2015.12.032.
[28] K. Chatterjee, M. Ashokkumar, H. Gullapalli, Y. Gong, Nitrogen-rich carbon nano-onions for oxygen reduction reaction, Carbon N Y 130 (2018) 645–651, https://doi.org/10.1016/j.carbon.2018.01.052.
[29] L.L. Sikeyi, T. Matthews, A.S. Adekunle, N.W. Maxakato, Electro-oxidation of ethanol and methanol on Pd/C, Pd/CNFs and Pd−Ru/CNFs nanocatalysts in alkaline direct alcohol fuel cell, Electroanalysis 32 (2020) 2681–2692, https://doi.org/10.1002/elan.202060260.
[30] L.L. Sikeyi, T.D. Ntuli, T.H. Mongwe, N.W. Maxakato, E. Carleschi, B.P. Doyle, N. J. Coville, M.S. Maubane-Nkadimeng, Microwave assisted synthesis of nitrogen doped and oxygen functionalized carbon nano onions supported palladium nanoparticles as hybrid anodic electrocatalysts for direct alkaline ethanol fuel cells, Int. J. Hydrogen Energy 46 (2021) 10862–10875, https://doi.org/10.1016/j.ijhydene.2020.12.154.
[31] V. Dhand, J.S. Prasad, M.V. Rao, S. Bharadwaj, Flame synthesis of carbon nano onions using liquefied petroleum gas without catalyst Flame synthesis of carbon nano onions using lique fi ed petroleum gas without catalyst. https://doi.org/10.1016/j.msec.2012.10.029, 2013.
[32] S. Fu, C. Zhu, D. Du, Y. Lin, Facile one-step synthesis of three-dimensional Pd-Ag bimetallic alloy networks and their electrocatalytic activity toward ethanol oxidation, ACS Appl. Mater. Interfaces 7 (2015) 13842–13848, https://doi.org/10.1021/acsami.5b01963.
[33] R. Kiyani, S. Rowshanzamir, M.J. Parnian, Nitrogen doped graphene supported palladium-cobalt as a promising catalyst for methanol oxidation reaction: synthesis, characterization and electrocatalytic performance, Energy 113 (2016) 1162–1173, https://doi.org/10.1016/j.energy.2016.07.143.
[34] A. Sahai, N. Goswami, Structural and optical investigations of oxygen defects in zinc oxide nanoparticles. https://doi.org/10.1063/1.4917664, 2014.
[35] A.M. Ferraria, A.P. Carapeto, A. Maria, X-ray photoelectron spectroscopy, Silver salts revisited 86 (2012) 1988–1991, https://doi.org/10.1016/j.vacuum.2012.05.031.
[36] M.A. Matin, A. Kumar, R.R. Bhosale, M.A.H. Saleh Saad, F.A. Almomani, M.J. Al-Marri, PdZn nanoparticle electrocatalysts synthesized by solution combustion for methanol oxidation reaction in an alkaline medium, RSC Adv. 7 (2017) 42709–42717, https://doi.org/10.1039/c7ra07013f.
[37] L. Lit, S. Yu, X. Yue, J. Wang, M. Liang, L. Goo, S. Yan, Effect of annealing atomic rearrangement on electrochemical performance of Pd-Ni catalyst, Int. J. Electrochem. Sci. 15 (2020) 7896–7913, https://doi.org/10.20964/2020.08.90.
[38] H. Bahruji, M. Bowker, G. Hutchings, N. Dimitratos, P. Wells, E. Gibson, W. Jones, C. Brookes, D. Morgan, G. Lalev, Pd/ZnO catalysts for direct CO2hydrogenation to methanol, J. Catal. 343 (2016) 133–146, https://doi.org/10.1016/j.jcat.2016.03.017.
[39] J. Shi, J. Wang, Y. Chen, Y. Sun, B. Liu, Y. Fan, Ag-Pd core–shell electrocatalysts for ethanol oxidation and oxygen reduction reactions in alkaline medium, JPhys Materials 4 (2021), https://doi.org/10.1088/2515-7639/abc733.
[40] O.A. Ojelade, S.F. Zaman, Co2 hydrogenation to methanol over PdZn/CeO2 catalyst, Comptes Rendus de L'Academie Bulgare Des Sciences 72 (2019) 732–739, https://doi.org/10.7546/CRABS.2019.06.05.
[41] Y. Zhang, Y. Liao, G. Shi, W. Wang, B. Su, Preparation, characterization, and catalytic performance of Pd-Ni/AC bimetallic nano-catalysts, Green Process. Synth. 9 (2020) 760–769, https://doi.org/10.1515/gps-2020-0071.
[42] S. Sankar, N. Watanabe, G.M. Anilkumar, B.N. Nair, S.G. Sivakamiammal, T. Tamaki, T. Yamaguchi, Electro-oxidation competency of palladium nanocatalysts over ceria-carbon composite supports during alkaline ethylene glycol oxidation, Catal. Sci. Technol. 9 (2019) 493–501, https://doi.org/10.1039/c8cy02232a.
[43] A. Elsheikh, J. McGregor, Synthesis and characterization of pdagni/c trimetallic nanoparticles for ethanol electrooxidation, Nanomaterials 11 (2021), https://doi.org/10.3390/nano11092244.
[44] L. Lai, G. Yang, Q. Zhang, H. Yu, F. Peng, Essential analysis of cyclic voltammetry of methanol electrooxidation using the differential electrochemical mass spectrometry, J. Power Sources 509 (2021) 230397, https://doi.org/10.1016/j.jpowsour.2021.230397.
[45] S. Roy, S. Payra, S. Challagulla, R. Arora, S. Roy, C. Chakraborty, Enhanced photoinduced electrocatalytic oxidation of methanol using Pt nanoparticle-decorated TiO2-polyaniline ternary nanofibers, ACS Omega 3 (2018) 17778–17788, https://doi.org/10.1021/acsomega.8b02610.
[46] S. Ali, R. Ahmed, M.S. Ansari, Evaluation of stability and catalytic activity of direct methanol fuel cell nano-catalysts by cyclic voltammetry, NUST Journal of Engineering Sciences (NJES) 6 (2013) 21–26.
[47] N. Roy, S. Yasmin, A. Ejaz, H. Soon Han, S. Jeon, Influence of pyrrolic and pyridinic-N in the size and distribution behaviour of Pd nanoparticles and ORR mechanism, Appl. Surf. Sci. 533 (2020), https://doi.org/10.1016/j.apsusc.2020.147500.
[48] L. Yang, Y. Wang, H. Feng, H. Zeng, C. Tan, J. Yao, J. Zhang, L. Jiang, Y. Sun, PdAg nanoparticles with different sizes: facile one-step synthesis and high electrocatalytic activity for formic acid oxidation, Chem. Asian J. 16 (2021) 34–38, https://doi.org/10.1002/asia.202001253.
[49] H. Ay, F. Sen, Metal, metal oxides, and metal sulfide roles in fuel cell, in: metal, metal-oxides and metal sulfides for batteries, Fuel Cells, Solar Cells, Photocatalysis and Health Sensors (2021) 115–145. Springer.
[50] M.A. Matin, A. Kumar, R.R. Bhosale, M.A.H. Saleh Saad, F.A. Almomani, M.J. Al-Marri, PdZn nanoparticle electrocatalysts synthesized by solution combustion for methanol oxidation reaction in an alkaline medium, RSC Adv. 7 (2017) 42709–42717, https://doi.org/10.1039/c7ra07013f.
[51] S. Amirinejad, J.B. Parsa, Promotion of catalytic activity of Pt@Al-Ti doped ZnO nanostructured anodes for direct methanol fuel cells, J. Solid State Electrochem. 27 (2023) 2347–2363, https://doi.org/10.1007/s10008-023-05491-0.
[52] Y. Wang, Z.M. Sheng, H. Yang, S.P. Jiang, C.M. Li, Electrocatalysis of carbon black- or activated carbon nanotubes-supported Pd-Ag towards methanol oxidation in alkaline media, Int. J. Hydrogen Energy 35 (2010) 10087–10093, https://doi.org/10.1016/j.ijhydene.2010.07.172.
[53] J.M. Léger, S. Rousseau, C. Coutanceau, F. Hahn, C. Lamy, How bimetallic electrocatalysts does work for reactions involved in fuel cells?: example of ethanol oxidation and comparison to methanol, in: Electrochim Acta, 2005, pp. 5118–5125, https://doi.org/10.1016/j.electacta.2005.01.051.
[54] U.B. Demirci, Theoretical means for searching bimetallic alloys as anode electrocatalysts for direct liquid-feed fuel cells, J. Power Sources 173 (2007) 11–18, https://doi.org/10.1016/j.jpowsour.2007.04.069.
[55] J. Greeley, J.K. Nørskov, A general scheme for the estimation of oxygen binding energies on binary transition metal surface alloys, Surf. Sci. 592 (2005) 104–111, https://doi.org/10.1016/j.susc.2005.07.018.
[56] Z. Teng, M. Li, Z. Li, Z. Liu, G. Fu, Y. Tang, Facile synthesis of channel-rich ultrathin palladium-silver nanosheets for highly efficient formic acid electrooxidation, Mater. Today Energy 19 (2021), https://doi.org/10.1016/j.mtener.2020.100596.
[57] C. Te Hsieh, J.Y. Lin, S.Y. Yang, Carbon nanotubes embedded with PtRu nanoparticles as methanol fuel cell electrocatalysts, Physica E Low Dimens Syst Nanostruct 41 (2009) 373–378, https://doi.org/10.1016/j.physe.2008.08.060.
[58] Y. Qiu, J. Zhang, J. Jin, J. Sun, H. Tang, Q. Chen, Z. Zhang, W. Sun, G. Meng, Q. Xu, Y. Zhu, A. Han, L. Gu, D. Wang, Y. Li, Construction of Pd-Zn dual sites to enhance the performance for ethanol electro-oxidation reaction, (n.d.). https://doi.org/10.1038/s41467-021-25600-9..
[59] I. Petriev, P. Pushankina, I. Lutsenko, N. Shostak, M. Baryshev, Synthesis, electrocatalytic and gas transport characteristics of pentagonally structured star-shaped nanocrystallites of pd-ag, Nanomaterials 10 (2020) 1–19, https://doi.org/10.3390/nano10102081.
[60] S. Ghosh, S. Bysakh, R.N. Basu, Bimetallic Pd96Fe4 nanodendrites embedded in graphitic carbon nanosheets as highly efficient anode electrocatalysts, Nanoscale Adv. 1 (2019) 3929–3940, https://doi.org/10.1039/c9na00317g.
[61] K.M. Hassan, A.A. Hathoot, R. Maher, M. Abdel Azzem, Electrocatalytic oxidation of ethanol at Pd, Pt, Pd/Pt and Pt/Pd nano particles supported on poly 1,8-diaminonaphthalene film in alkaline medium, RSC Adv. 8 (2018) 15417–15426, https://doi.org/10.1039/c7ra13694c.
[62] J. Jiang, A. Kucernak, Electrooxidation of small organic molecules on mesoporous precious metal catalysts II: CO and methanol on platinum-ruthenium alloy, J. Electroanal. Chem. 543 (2003) 187–199, https://doi.org/10.1016/S0022-0728(03)00046-9.
[63] J.W. Guo, T.S. Zhao, J. Prabhuram, R. Chen, C.W. Wong, Preparation and characterization of a PtRu/C nanocatalyst for direct methanol fuel cells, Electrochim. Acta 51 (2005) 754–763, https://doi.org/10.1016/j.electacta.2005.05.056.
[64] T. Matthews, M.P. Chabalala, S.P. Mbokazi, T. Maumau, K. Mugadza, J. Gallenberger, J.P. Hofmann, T.H. Dolla, N.W. Maxakato, Multi-dimensional PtRu/Co3O4-Activated carbon Nano-Electrocatalyst: metal–Support Interaction,

and electronic contributions towards methanol electrooxidation in alkaline fuel cells, Fuel 359 (2024), https://doi.org/10.1016/j.fuel.2023.130460.

[65] D. Morales-Acosta, D. López de la Fuente, L.G. Arriaga, G. Vargas Gutiérrez, F. J. Rodríguez Varela, Electrochemical investigation of Pt-Co/MWCNT as an alcohol-tolerant ORR catalyst for direct oxidation fuel cells, Int. J. Electrochem. Sci. 6 (2011) 1835–1854.

[66] A.K. Ipadeola, R. Barik, S.C. Ray, K.I. Ozoemena, Bimetallic Pd/SnO2 nanoparticles on metal organic framework (MOF)-Derived carbon as electrocatalysts for ethanol oxidation, Electrocatalysis 10 (2019) 366–380, https://doi.org/10.1007/s12678-019-00518-5.

[67] R.M. Abdel Hameed, Enhanced ethanol electro-oxidation reaction on carbon supported Pd-metal oxide electrocatalysts, J. Colloid Interface Sci. 505 (2017) 230–240, https://doi.org/10.1016/j.jcis.2017.05.095.

[68] F. Seland, R. Tunold, D.A. Harrington, Impedance study of methanol oxidation on platinum electrodes, Electrochim. Acta 51 (2006) 3827–3840, https://doi.org/10.1016/j.electacta.2005.10.050.

[69] S. Lyu, Y. Zhang, Z. Li, X. Liu, Z. Tian, C. Liu, J. Li, L. Wang, Electronic metal-support interactions between CuxO and ZnO for CuxO/ZnO catalysts with enhanced CO oxidation activity, Front. Chem. 10 (2022), https://doi.org/10.3389/fchem.2022.912550.

[70] T. Pajkossy, R. Jurczakowski, Electrochemical impedance spectroscopy in interfacial studies, Curr. Opin. Electrochem. 1 (2017) 53–58, https://doi.org/10.1016/j.coelec.2017.01.006.